



Decoupling Strategy for Three-phase Photovoltaic Grid-connected Inverters Based on Double Closed-loop Strategy

Jiayi Zhao

Logistics Engineering College, Shanghai Maritime University, Shanghai 201306, Shanghai, China

202210234059@stu.shmtu.edu.cn

Abstract. With the increasing penetration of distributed photovoltaic (PV) systems, grid-connected PV inverters must achieve rapid, accurate, and low-harmonic power injection across a wide operating range. Conventional control methods in the abc stationary reference frame exhibit significant steady-state errors and severe AC coupling effects, failing to meet high power quality requirements. To address the power tracking accuracy and dynamic response challenges in three-phase PV inverters, this paper proposes a dual-loop control strategy implemented in the dq rotating reference frame, consisting of an outer power loop and an inner current loop. By converting AC quantities into DC components through dq transformation, and incorporating grid voltage feed-forward and feed-forward decoupling compensation, independent active/reactive power control is achieved. Simulation results demonstrate rapid power response without steady-state error during dynamic processes—where active power (P) increases from 2.5 kW to 5 kW at 0.1 s and reactive power (Q) rises from 0 kVA to 3 kVA at 0.2 s, verifying the effectiveness and stability of the proposed control strategy.

Keywords: Grid-Connected Photovoltaic Inverter, Dual-Loop Control, Voltage Feed-forward, Feed-forward Decoupling, Power Control.

1 Introduction

With the accelerated implementation of China's Dual Carbon Initiative, grid penetration of photovoltaic systems and other renewable energy sources has witnessed sustained growth. Under these circumstances, three-phase grid-connected PV inverters - serving as critical power conversion interfaces - play a decisive role in maintaining grid power quality and operational stability. Nevertheless, conventional control strategies demonstrate fundamental limitations in achieving precise d-q current tracking in three-phase inverters, consequently leading to elevated grid harmonics, compromised dynamic performance, and potential system instability.

To address issues such as reduced stability margin and deteriorated dynamic performance caused by power coupling, Li et al. proposed a universal analytical model for power coupling in grid-forming converters, providing a quantitative tool for

evaluating power coupling characteristics across different grid-forming control strategies [1]. Zhao et al. suggests that the virtual inductor (VI) technique can be applied to increase the coupling impedance between the converter and the grid, thereby enhancing the stability margin [2]. However, an excessively large virtual inductor may lead to an increase in the power angle and potentially cause loss of synchronization [3]. Moreover, proceeding from this basis, Wen et al. introduced a strategy employing virtual inductance exclusively in the q-axis, aiming to achieve improved steady-state decoupling [4]. Considering the impact of line impedance variations on the performance of decoupling controllers, Dong et al. proposed a decoupling method based on an extended state observer (ESO), which enhances the robustness of the decoupling control system [5]. The existing approaches, while making significant theoretical contributions, still face substantial implementation barriers in real-world V2G applications, particularly in addressing dynamic power interactions and maintaining system stability under rapid power flow reversals [6].

Building upon the aforementioned research, this paper first analyzes the coupling characteristics of d-axis and q-axis currents based on the mathematical model of a three-phase full-bridge inverter in the dq rotating reference frame, elucidating the necessity of decoupling control. On the foundation of traditional PI control, the proposed method incorporates grid voltage feed-forward and cross-decoupling compensation to counteract coupling components, thereby achieving independent current control dynamically. The simulation analysis verified the superior performance of the proposed control strategy. Bode diagram analysis shows that the compensated current loop and voltage loop ensure the stability of the system. The active power waveform indicates that there is no oscillation in the dynamic process. The reactive power waveform verified the effectiveness of the feed-forward feedback hybrid decoupling strategy.

2 Mathematical Modeling of Three-phase Full-bridge Inverter

The core of electric vehicle (EV) charging/discharging systems based on V2G technology lies in the design of bidirectional AC-DC converters [7]. The report adopts a typical three-phase full-bridge inverter topology [8].

First, the mathematical model of the micro-grid energy storage inverter is established for the grid-connected scenario [9]. Selecting the filter inductor current as the state variable, the governing equations are derived as shown in Equation (1):

$$L_f \begin{bmatrix} \frac{di_a}{dt} \\ \frac{di_b}{dt} \\ \frac{di_c}{dt} \end{bmatrix} = \begin{bmatrix} v_{a0} \\ v_{b0} \\ v_{c0} \end{bmatrix} - \begin{bmatrix} v_a \\ v_b \\ v_c \end{bmatrix} - r \begin{bmatrix} i_{ia} \\ i_{ib} \\ i_{ic} \end{bmatrix} \quad (1)$$

Where L_f represents the filter inductance; r represents the parasitic resistance of the filter inductor. All three-phase filter inductors share identical parameters.

In the abc stationary frame, only two of the three phase variables are independent due to the zero-sequence constraint, requiring control of these sinusoidal AC

quantities, which complicates implementation. For balanced three-phase three-wire systems, the Clarke transformation simplifies analysis by converting the variables into two-phase stationary coordinates. The mathematical model of the micro-grid energy storage inverter in the $\alpha\beta$ reference frame can be derived as Equation (2):

$$L_f \begin{bmatrix} \frac{di_\alpha}{dt} \\ \frac{di_\beta}{dt} \end{bmatrix} = \begin{bmatrix} v_{\alpha 0} \\ v_{\beta 0} \end{bmatrix} - \begin{bmatrix} v_\alpha \\ v_\beta \end{bmatrix} - r \begin{bmatrix} i_\alpha \\ i_\beta \end{bmatrix} \quad (2)$$

Where L_f is the filter inductance; i_α and i_β are the output current components in the two-phase $\alpha\beta$ coordinate system; di_α/dt and di_β/dt are the time derivatives of the current components, representing the current change rate; $v_{\alpha 0}$ and $v_{\beta 0}$ are the output voltage components of the inverter in the $\alpha\beta$ coordinate system; v_α and v_β are the voltage components on the load side; r is the equivalent resistance.

To achieve zero error, the proposed method uses Clark and Park transformations to convert the system into a synchronous rotating dq frame. This frame rotates counterclockwise at angular velocity ω .

The Park transformation matrix equation is:

$$\begin{bmatrix} v_d \\ v_q \end{bmatrix} = \begin{bmatrix} \cos \omega t & \sin \omega t \\ -\sin \omega t & \cos \omega t \end{bmatrix} \begin{bmatrix} v_\alpha \\ v_\beta \end{bmatrix} \quad (3)$$

By combining Equation (2) and Equation (3), the expression of the microgrid energy storage inverter in the dq coordinate system can be obtained, as shown in Equation (4).

$$\begin{cases} L_f \frac{di_d}{dt} = v_{d0} - v_d + \omega L_f i_q - r i_d \\ L_f \frac{di_q}{dt} = v_{q0} - v_q - \omega L_f i_d - r i_q \end{cases} \quad (4)$$

3 Virtual Decoupling Control Strategy

From Equation (4), it can be observed that there is a coupling relationship between the d-axis and q-axis. Therefore, a decoupling control strategy needs to be introduced. The components of the inverter voltage control vector in the d-axis and q-axis directions are expressed as:

$$\begin{cases} v_d = u_{gd} + \omega L_f i_q - \Delta v_d \\ v_q = u_{gq} - \omega L_f i_d - \Delta v_q \end{cases} \quad (5)$$

Where Δv_d and Δv_q are the outputs of the d-axis and q-axis current loops respectively.

When a PI regulator is employed in the current loop, they satisfy:

$$\begin{cases} \Delta v_d = (K_{ip} + \frac{K_{ii}}{s})(i_d^* - i_d) \\ \Delta v_q = (K_{ip} + \frac{K_{ii}}{s})(i_q^* - i_q) \end{cases} \quad (6)$$

Where K_{ip} and K_{ii} are the proportional and integral coefficients of the current PI regulator, respectively; i_d^* and i_q^* are the reference currents of the d-axis and q-axis, respectively; and i_d and i_q are the sampled actual currents of the d-axis and q-axis, respectively.

Substituting Equation (6) into Equation (5) yields Equation (7):

$$\begin{cases} L \frac{di_d}{dt} = -ri_d + \Delta v_d \\ L \frac{di_q}{dt} = -ri_q + \Delta v_q \end{cases} \quad (7)$$

Equation (7) proves that current feedback terms eliminate coupled current components, enabling independent d/q-axis current control. Grid voltage feed-forward terms are added to improve dynamic response [10]. As shown in Fig. 1, each PI controller's output includes a decoupling component that counteracts the actual coupling effect with equal magnitude but opposite phase, ensuring effective decoupling.

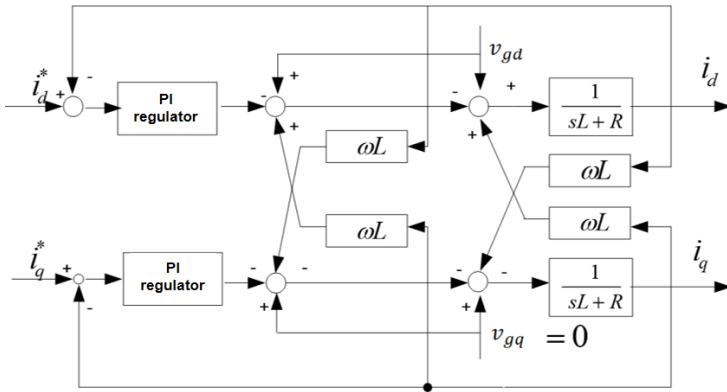


Fig. 1. Current decoupling control diagram. (Picture credit: Original)

The d-axis current and q-axis current are controlled separately, with the control scheme illustrated in Fig. 2. In Fig.2, T_s represents the sampling period of the inductor current. K_p and K_{ii} are the PI parameters of the respective current loops. $1/(1+0.5T_s s)$ represents the inertial delay introduced by PWM control. $1/(1+T_s s)$ represents the delay in current sampling. $K_{PWM} = 1$ is the modulation index. Given the switching frequency and device parameters as: $T_s = 1/f_s = 1/15 \text{ kHz} = 66.7 \text{ us}$, $L = 1.5\text{mH}$, $R = 0.1\Omega$, $C = 50\text{uF}$.

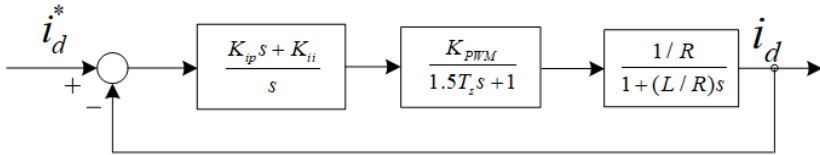


Fig. 2. Simplified structure block diagram of the D-axis current loop. (Picture credit: Original)

4 Simulation Analysis

To validate the correctness and effectiveness of the proposed topology and its control strategy, a simulation model was implemented in Simulink based on the aforementioned modelling and control parameter design methodology.

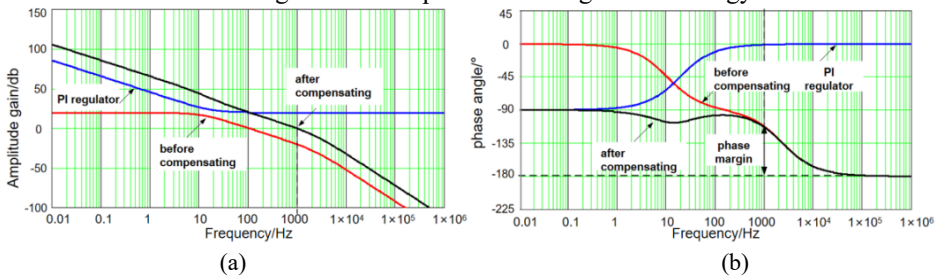


Fig. 3. Bode plots before and after current loop compensation, (a) Amplitude-frequency characteristic diagram; (b) Phase-frequency characteristic diagram. (Picture credit: Original)

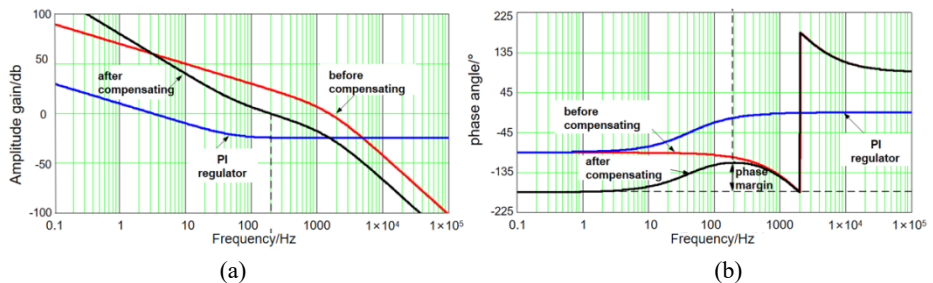


Fig. 4. Bode plots before and after voltage loop compensation, (a) Amplitude-frequency characteristic diagram; (b) Phase-frequency characteristic diagram. (Picture credit: Original)

Fig. 3 and Fig. 4 are the Bode plots before and after current and voltage loop compensation. Table 1 and Table 2 yield the summarized results presented in Fig. 3 and Fig. 4.

Table 1 demonstrates that the uncompensated current loop's open-loop transfer function $G_{c0}(s)$ exhibits a low-frequency gain of 20dB, crosses the 0dB line at 100Hz with a phase margin of 75°. After compensation implementation, the closed-loop transfer function $G_{il}(s)$ of the current loop shows its magnitude-frequency characteristic curve crossing the 0dB line at 1000Hz with a -20dB/decade slope, while maintaining a phase margin of 60°.

Table 1. Data before and after current loop compensation.
(Data from: this study)

Index	Before compensation (open-loop transfer function $G_{c0}(s)$)	After compensation (closed-loop transfer function $G_{il}(s)$)
Low-frequency band gain	20 dB	/
Crossing frequency (0dB point)	100 Hz	1000 Hz
Phase margin	75°	60°
Slope of amplitude-frequency characteristic	/	-20 dB/dec

As evidenced in Table 2, the uncompensated voltage loop's original gain function $G_{v0}(s)$ crosses the 0dB line at 2kHz. Following the implementation of the compensation network, the magnitude-frequency characteristic crosses the 0dB line at 150Hz with a -20dB/decade slope while maintaining a 55° phase margin.

Table 2. Data before and after voltage loop compensation.
(Data from: this study)

Index	Before compensation (open-loop transfer function $G_{c0}(s)$)	After compensation (closed-loop transfer function $G_{il}(s)$)
Crossing frequency (0dB point)	2 kHz	150 Hz
Slope of amplitude-frequency characteristic	/	-20 dB/dec
Phase margin	/	55°

This analysis demonstrates that in the current loop design, the incorporation of grid voltage feed-forward components significantly enhances the system's dynamic response capability to grid voltage fluctuations. Meanwhile, the voltage outer-loop design ensures steady-state output voltage accuracy. Although exhibiting relatively slower initial dynamic response, the optimized PI parameters achieve overall system performance optimization.

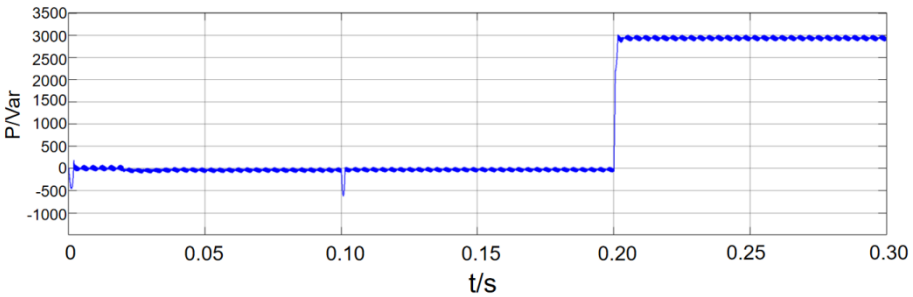


Fig. 5. Active power waveform. (Picture credit: Original)

Fig. 5 verifies that the proposed dq-decoupled current loop can eliminate cross-coupling terms in real time, with no power curve oscillations or secondary regulation phenomena observed during dynamic processes. The adaptive PI parameters maintain constant phase margin across wide power ranges, ensuring the active power channel achieves rapid static-error-free tracking during disturbances. This solution provides reliable power control support for high-penetration renewable energy grid integration.

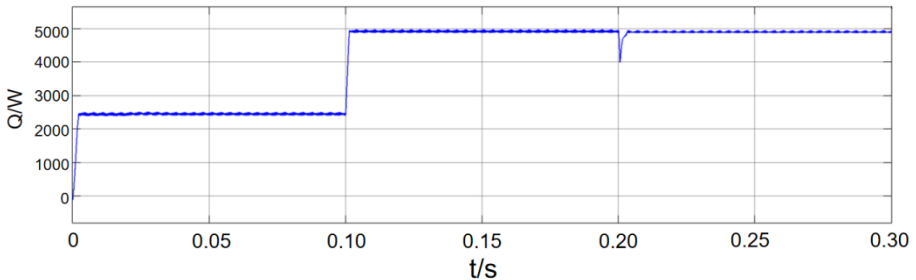


Fig. 6. Reactive power waveform. (Picture credit: Original)

Fig. 6 validates the effectiveness of the proposed dq-axis feed-forward-feedback hybrid decoupling strategy. By implementing real-time feed-forward compensation of cross-coupling terms to the q-axis voltage reference, combined with adaptive PI parameter tuning, the reactive power channel maintains independent and non-static-error regulation capability even under grid voltage fluctuations or V2G bidirectional power scenarios. This approach provides a low-complexity, high-robustness technical solution for the coordinated grid integration of high-penetration renewable energy and electric vehicles.

5 Conclusion

This paper addresses the critical challenges of large steady-state errors, sluggish dynamic response, and power coupling in three-phase grid-connected photovoltaic (PV) inverters under conventional control strategies. A novel dual-loop decoupling control strategy incorporating voltage feed-forward compensation and current dynamic decoupling is proposed, enabling high-precision and fast-response power regulation.

Theoretical analysis and simulation results demonstrate that the method effectively eliminates dq-axis current coupling, delivers rapid dynamic response without overshoot or oscillation, and reduces steady-state error to near zero. Bode plot analysis reveals significant performance improvements: the compensated current loop's crossover frequency increases from 100 Hz to 1000 Hz while maintaining a 60° phase margin, and the voltage loop's crossover frequency is optimized to 150 Hz, substantially enhancing system stability.

Furthermore, this strategy reduces control complexity while maintaining superior dynamic performance, providing a reliable solution for high-penetration renewable energy integration. Future research will focus on optimizing parameter self-adaptation algorithms to enhance robustness under complex grid conditions.

References

1. Li, M., Wang, Y., Hu, W. et al.: Unified modeling and analysis of dynamic power coupling for grid-forming converters. *IEEE Trans. Power Electron.* 37(2), 2321–2337 (2022).
2. Zhao, F., Zhu, T., Li, Z., Wang, X.: Low-frequency resonances in grid-forming converters: causes and damping control. *IEEE Trans. Power Electron.* 39(11), 14430–14447 (2024).
3. Yang, Y., Xu, J., Li, C. et al.: A new virtual inductance control method for frequency stabilization of grid-forming virtual synchronous generators. *IEEE Trans. Ind. Electron.* 70(1), 441–451 (2023).
4. Wen, T., Zhu, D., Zou, X., Jiang, B., Peng, L., Kang, Y.: Power coupling mechanism analysis and improved decoupling control for virtual synchronous generator. *IEEE Trans. Power Electron.* 36(3), 3028–3041 (2021).
5. Dong, N., Li, M., Chang, X., Zhang, W., Yang, H., Zhao, R.: Robust power decoupling based on feedforward decoupling and extended state observers for virtual synchronous generator in weak grid. *IEEE J. Emerg. Sel. Top. Power Electron.* 11(1), 576–587 (2023).
6. Du, W., Chen, X., Wang, H.F.: Power system electromechanical oscillation modes as affected by dynamic interactions from grid-connected PMSGs for wind power generation. *IEEE Trans. Sustain. Energy* 8(3), 1301–1312 (2017).
7. Fahem, K., Chariag, D. E., Sbita, L.: On-board bidirectional battery chargers topologies for plug-in hybrid electric vehicles. In: 2017 International Conference on Green Energy Conversion Systems (GECS), pp. 1 – 6. IEEE, Hammamet, Tunisia (2017).
8. Rodriguez, P., Pou, J., Bergas, J., Candela, J.I., Burgos, R.P., Boroyevich, D.: Decoupled double synchronous reference frame PLL for power converters control. *IEEE Trans. Power Electron.* 22(2), 584–592 (2007).
9. Li, Y., Li, X., Liu, Y., Wang, X.: Optimization of grid-forming energy storage systems to enhance sending-end power system stability. In: 2025 8th International Conference on Energy, Electrical and Power Engineering (CEEPE), pp. 1319–1324. IEEE, Wuxi, China (2025).
10. Lu, G., Sun, Z., Meng, X.: Voltage feed-forward control strategy for virtual synchronous motor. In: 2022 9th International Forum on Electrical Engineering and Automation (IFEFA), pp. 964–968. IEEE, Zhuhai, China (2022).

Open Access This chapter is licensed under the terms of the Creative Commons Attribution-NonCommercial 4.0 International License (<http://creativecommons.org/licenses/by-nc/4.0/>), which permits any noncommercial use, sharing, adaptation, distribution and reproduction in any medium or format, as long as you give appropriate credit to the original author(s) and the source, provide a link to the Creative Commons license and indicate if changes were made.

The images or other third party material in this chapter are included in the chapter's Creative Commons license, unless indicated otherwise in a credit line to the material. If material is not included in the chapter's Creative Commons license and your intended use is not permitted by statutory regulation or exceeds the permitted use, you will need to obtain permission directly from the copyright holder.

